Faraday Discussions

Cite this: *Faraday Discuss.*, 2023, **242**, 443

ROYAL SOCIETY OF CHEMISTRY

PAPER

View Article Online
View Journal | View Issue

The role of the gold–platinum interface in AuPt/TiO_2-catalyzed plasmon-induced reduction of CO_2 with water†

Leila Hammoud,[a] Claire Strebler,[a] Joumana Toufaily,[b] Tayssir Hamieh,[bc] Valérie Keller[a] and Valérie Caps *[a]

Received 10th May 2022, Accepted 8th July 2022
DOI: 10.1039/d2fd00094f

Bimetallic gold–platinum nanoparticles have been widely studied in the fields of nanoalloys, catalysis and plasmonics. Many preparation methods can lead to the formation of these bimetallic nanoparticles (NPs), and the structure and related properties of the nanoalloy often depend on the preparation method used. Here we investigate the ability of thermal dimethylformamide (DMF) reduction to prepare bimetallic gold–platinum sub-nm clusters supported on titania. We find that deposition of Pt preferentially occurs on gold. Formation of sub-nm clusters (*vs.* NPs) appears to be dependent on the metal concentration used: clusters can be obtained for metal loadings up to 4 wt% but 7–8 nm NPs are formed for metal loadings above 8 wt%, as shown using high resolution transmission electron microscopy (HRTEM). X-ray photoelectron spectroscopy (XPS) shows electron-rich Au and Pt components in a pure metallic form and significant platinum enrichment of the surface, which increases with increasing Pt/Au ratio and suggests the presence of Au@Pt core–shell type structures. By contrast, titania-supported bimetallic particles (typically >7 nm) obtained by sodium borohydride ($NaBH_4$) reduction in DMF, contain Au/Pt Janus-type objects in addition to oxidized forms of Pt as evidenced by HRTEM, which is in agreement with the lower Pt surface enrichment found by XPS. Both types of supported nanostructures contain a gold–platinum interface, as shown by the chemical interface damping, *i.e.* gold plasmon damping by Pt, found using UV-visible spectroscopy. Evaluation of the materials for plasmon-induced continuous flow CO_2 reduction with water, shows that: (1) subnanometer metallic clusters are not suitable for CO_2 reduction with water, producing hydrogen from the competing water reduction instead, thereby highlighting the plasmonic nature of the reaction; (2) the highest methane production rates are

[a]*ICPEES (CNRS UMR 7515/Université de Strasbourg), 25 rue Becquerel, 67087 Strasbourg, Cedex 02, France. E-mail: caps@unistra.fr*

[b]*Laboratory of Materials, Catalysis, Environment and Analytical Methods Laboratory (MCEMA), Faculty of Sciences, Lebanese University, Rafic Hariri Campus, Hadath, Lebanon*

[c]*Faculty of Science and Engineering, Maastricht University, 6200 MD, Maastrich, P.O. Box 616, The Netherlands*

† Electronic supplementary information (ESI) available. See **https://doi.org/10.1039/d2fd00094f**

obtained for the highest Pt enrichments of the surface, *i.e.* the core–shell-like structures achieved by the thermal DMF reduction method; (3) selectivity towards CO_2 reduction *vs.* the competing water reduction is enhanced by loading of the plasmonic NPs, *i.e.* coverage of the titania semi-conductor by plasmonic NPs. Full selectivity is achieved for loadings above 6 wt%, regardless of the NPs composition and alloy structure.

Introduction

Nanoalloys and bimetallic nanoparticles have been widely studied because their size restriction and high surface to volume ratio may lead to unique properties that differ from that of bulk alloys.[1–3] Besides, they may exhibit improved performance in comparison to their monometallic counterparts. In particular, bimetallic gold–platinum nanoparticles (NPs) have attracted a lot of interest in the fields of catalysis,[4,5] electrocatalysis,[6–14] sensors,[15–17] and more recently in the field of photocatalysis[18–20] and plasmonics.[21–23] Amongst the improved properties that lead to improved performances, one can cite improved CO tolerance that leads to more stable oxidation (electro)catalysts, electron transfers between Au and Pt which leads to more active catalysts. These properties mostly depend on the structure of the nanoalloy, and in particular on whether Pt and Au atoms are homogeneously mixed within the NP (solid solution) or Pt and Au phases are segregated in core–shell or raspberry-type structures. Both types of structure can be synthesized at the nanoscale. Nanostructures are controlled by the method and conditions used during their synthesis, and can be finely tuned.[19,24]

A large number of the methods developed to produce AuPt nanoalloys are based on the reduction of solubilized metal salts. In these methods, size and structure of the resulting bimetallic NPs are determined by the kinetics of nucleation *vs.* growth for each metal, thus by the reduction kinetics, which depend on the reducing agent, solvent, temperature and possible presence of surfactant to enhance size control. The most common reductants include sodium borohydride,[25–30] sodium citrate,[31] ascorbic acid,[32,33] hydrogen, hydroxylamine,[34] ethanol.

In 2008–2010, size-controlled monometallic gold clusters, *i.e.* sub-nanometer Au NPs, were synthesized by heating up a dimethylformamide (DMF) solution of a gold salt to 140 °C, in the absence of any additional reducing or stabilizing agent.[35,36] It was shown that at this temperature, this common organic solvent could be used as both reductant and stabilizer to produce monometallic gold clusters. This protocol was later applied to the synthesis of surfactant-free, DMF-stabilized platinum,[37] palladium,[38] copper [39] and iridium [40] clusters. The main characteristics and advantages of this method are the subnanometer size control achieved and the high purity of the colloidal solution produced (DMF-stabilized metal NPs).[41] These colloidal solutions can thus straight-forwardly be used as catalysts for a variety of key organic reactions, without the need for any purification step or immobilization of the colloids. To the best of our knowledge, immobilization of these colloids on inorganic powders has never been investigated before.

Here we investigate the ability of this method to produce supported clusters in one pot, by performing the thermal DMF reduction of metal salts in the presence of titania powder. We focus on the synthesis of titania-supported Au, Pt and Au–Pt

clusters and on the plasmon-induced catalytic properties of the resulting materials for the continuous gas phase photoreduction of CO_2 with water (eqn (1), (2a), (2b)).[42–44]

$$4H_2O + 8h^+ \rightarrow 2O_2 + 8H^+ \quad (1)$$

$$CO_2 + 8H^+ + 8e^- \rightarrow CH_4 + 2H_2O \quad (2a)$$

$$2H^+ + 2e^- \rightarrow H_2 \quad (2b)$$

We have recently shown that Au/TiO_2 shows some activity for this reaction under visible light ($\lambda > 420$ nm), *i.e.* under plasmonic excitation of the localized surface plasmon resonance (LSPR) of Au NPs.[28] The activity was however about 2 orders of magnitude lower than that observed under solar irradiation, *i.e.* upon additional activation of the semi-conductor (SC) support (titania). We here show that the titania-supported Au–Pt alloys obtained by thermal DMF reduction improves plasmon-induced CH_4 production rates by one order of magnitude. By comparing with titania-supported Au, Pt and Au–Pt NPs produced by $NaBH_4$ reduction of gold and platinum salts in DMF, we further uncover interesting effects of size, loading and composition of the bi-metallic NPs in plasmon-induced CO_2-to-CH_4 photoreduction with water.

Results and discussion

Bimetallic catalysts prepared by thermal DMF reduction

Deposition efficiency. Five catalysts were prepared with this method: the two monometallic $Au5/TiO_2$ and $Pt5/TiO_2$ references, with a targeted metal loading of 5 wt%, as well as three bimetallic catalysts, with targeted metal loadings of 5, 10 and 15 wt% at the same targeted Pt/Au ratio of 1, namely $Au2.5Pt2.5/TiO_2$, $Au5Pt5/TiO_2$ and $Au7.5Pt7.5/TiO_2$. The actual loadings of gold and platinum achieved in the monometallic catalysts, *i.e.* 4.05% and 0.3%, respectively (Table 1), show that gold is quite efficiently deposited (deposition yield of 81%) while platinum on the other hand has little affinity with titania (deposition yield of only 6%), under the conditions used.

In the bimetallic catalysts, the actual loading of both metals, as measured by ICP, was found to be quite dependent on the nature of the metal, and for each metal, on the targeted metal loading, *i.e.* the initial metal concentration used (Table 1). Fig. 1a shows the deposition yields of Au and Pt as a function of their targeted loading. For gold, deposition yields vary between 51% and 84%. For platinum, deposition yields vary even more drastically, between 17% and 82%. The deposition of Pt is found to be particularly inefficient for the low loaded material ($Au2.5Pt2.5/TiO_2$), but it markedly increases (to 61–82%) for the other two materials ($Au5Pt5/TiO_2$ and $Au7.5Pt7.5/TiO_2$). Optimal deposition is achieved for $Au5Pt5/TiO_2$, in which more than 80% of the gold and the platinum present in the solution is deposited on TiO_2. It is noted that only 6% of Pt was deposited in the absence of gold, at the same initial concentration of Pt (*i.e.* in $Pt5/TiO_2$). The much higher deposition yield obtained in $Au5Pt5/TiO_2$ thus highlights the key role of gold in platinum deposition. It suggests that gold may act as a nucleation site for Pt, *i.e.* that Pt deposition occurs preferentially on Au rather than on TiO_2.

Table 1 Metal deposition and catalytic performance

	Metal deposition								Catalytic performances[a]		
	Au			Pt							
	Loading (wt%)	Target (wt%)	Deposition yield (%)	Loading (wt%)	Target (wt%)	Deposition yield (%)	Total M loading (wt%)	Pt/Au Molar ratio	r_{CH_4} (μmol h^{-1} g^{-1})	r_{H_2} (μmol h^{-1} g^{-1})	Selectivity (%)
DMF/140 °C											
$Au5/TiO_2$	4.05	5	81	0	0	—	4.05	0.00	0	4	0
$Au2.5Pt2.5/TiO_2$	1.9	2.5	77	0.4	2.5	17	2.3	0.22	1.5	18.2	25
$Au5Pt5/TiO_2$	4.2	5	84	4.1	5	82	8.3	0.98	5.5	0	100
$Au7.5Pt7.5/TiO_2$	3.8	7.5	51	4.6	7.5	61	8.4	1.22	7.8	0	100
$Pt5/TiO_2$	0	0	—	0.3	5	6	0.3	—	0.2	0	100
DMF/$NaBH_4$											
$Au35/TiO_2$	33.4	35	95	0.0	0	—	33.4	0.00	0.1	0	100
$Au34Pt1/TiO_2$	34	34	100	1.0	1	100	35.0	0.03	1.5	0	100
$Au30Pt5/TiO_2$	30	30	100	2.7	5	54	32.7	0.09	2.8	0	100
$Au17.5Pt17.5/TiO_2$	17.5	17.5	100	2.4	17.5	13	19.9	0.14	4.7	0	100
$Au3.5Pt3.5/TiO_2$	2.8	3.5	80	0.4	3.5	10	3.2	0.13	0.7	0.1	97
$Au5Pt30/TiO_2$	5	5	100	1.3	30	4	6.3	0.25	1.9	0	100
$Pt35/TiO_2$	0	0	—	15.8	35	45	15.8	—	3.3	0	100

[a] Averaged over 5 h of reaction under illumination ($\lambda > 400$ nm).

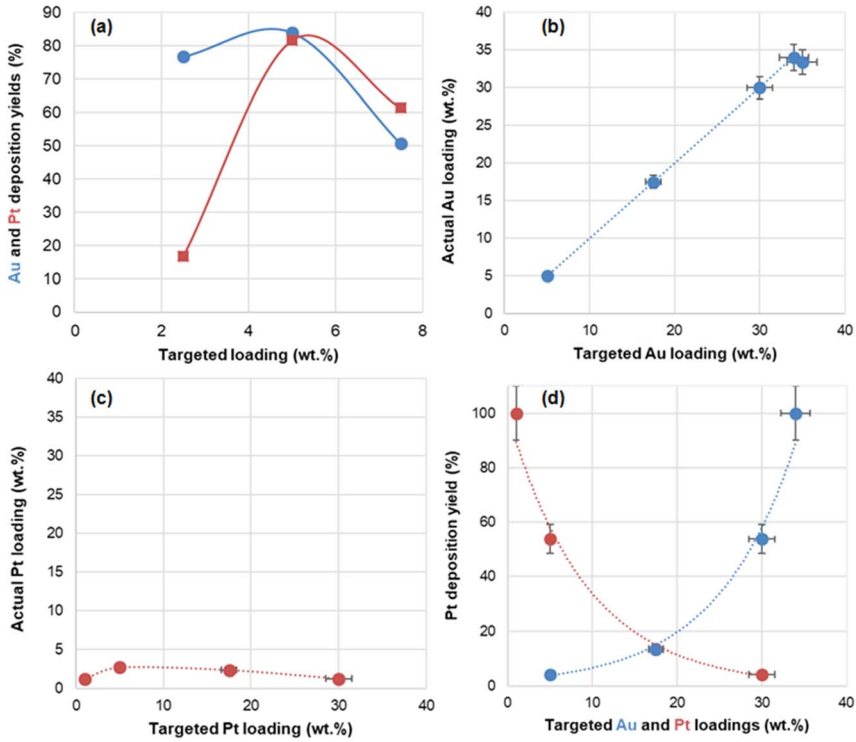

Fig. 1 Efficiency of the preparation methods. (a) DMF thermal reduction and (b–d) $NaBH_4$ reduction in DMF.

As a result of variations in deposition yields, the series of bimetallic catalysts prepared by thermal reduction in DMF consists of $AuPt/TiO_2$ materials with actual total metal loadings of 2.3, 8.3 and 8.4 wt% associated with increasing Pt/Au ratios of 0.22, 0.98 and 1.22, respectively.

Metal NPs size and distribution over titania. The materials were observed using scanning electron microscopy (SEM, Fig. 2). At low magnification, $Au5Pt5/TiO_2$ and $Au7.5Pt7.5/TiO_2$ distinctly show large metallic aggregates (white spots, Fig. 2c and d). It appears that the size of these large metallic aggregates increases with increasing target metal loading (from *ca.* 100 nm to 1 μm), while at the same time, the density of these metal aggregates over the granular titania support decreases. Metal aggregates are also observed on monometallic $Au5/TiO_2$ (Fig. 2a). On the other hand, no large aggregates are observed at this magnification over $Au2.5Pt2.5/TiO_2$ and $Pt5/TiO_2$ (Fig. 2b). Hence, formation of the large aggregates in the thermal DMF reduction process is likely favoured by increased concentration of the gold salt. At higher magnification, small metal NPs can be observed in both $Au5Pt5/TiO_2$ and $Au7.5Pt7.5/TiO_2$, with a high coverage of the granular TiO_2 support (Fig. 2c and d), but no metal NPs are observed in $Au2.5Pt2.5/TiO_2$, $Au5/TiO_2$ (Fig. 2a) or $Pt5/TiO_2$ (Fig. 2b).

Size distributions of the smallest metallic NPs present in $Au5Pt5/TiO_2$ and $Au7.5Pt7.5/TiO_2$ were obtained by measuring the dimensions of 200 of the smaller NPs in the TEM images (Fig. 3c and d). A significant amount of metal NPs exhibit

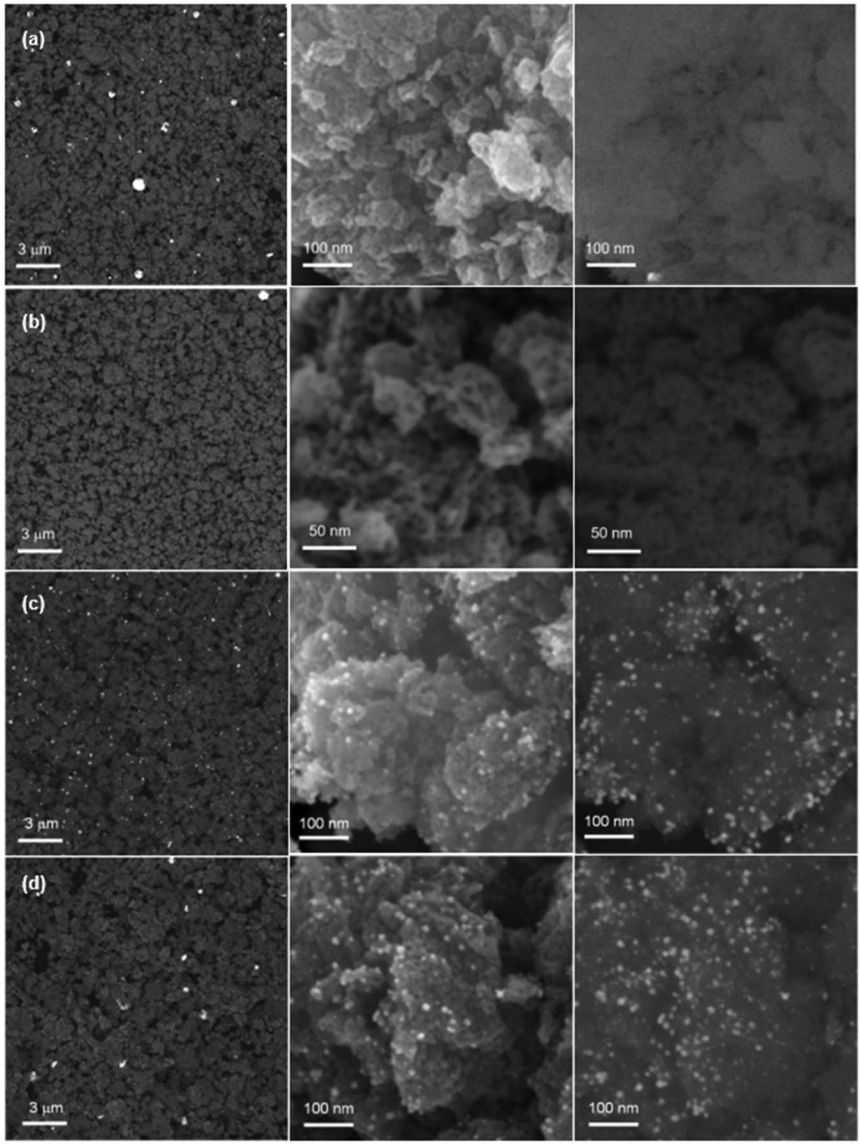

Fig. 2 SEM images of Au5/TiO_2 (a), Pt5/TiO_2 (b), Au5Pt5/TiO_2 (c), Au7.5Pt7.5/TiO_2 (d), at low magnification (left) and at high magnification, using In Lens (middle) and BSE (left, right) detectors.

an oblong shape. Size distributions are presented in Fig. 4b and c. Both materials exhibit rather large size distributions, centered at 5–6 nm, with mean NP sizes around 7.2 and 8.0 nm for Au5Pt5/TiO_2 and Au7.5Pt7.5/TiO_2, respectively. Notably, Au7.5Pt7.5/TiO_2 exhibits fewer NPs smaller than 3 nm (only 0.5% of the counted population *vs.* 8.5% in Au5Pt5/TiO_2) and more NPs larger than 10 nm, which represent about 25% of the counted population. However, no particles (in the 2–20 nm size range) could be detected on Au2.5Pt2.5/TiO_2, Au5/TiO_2 and Pt5/

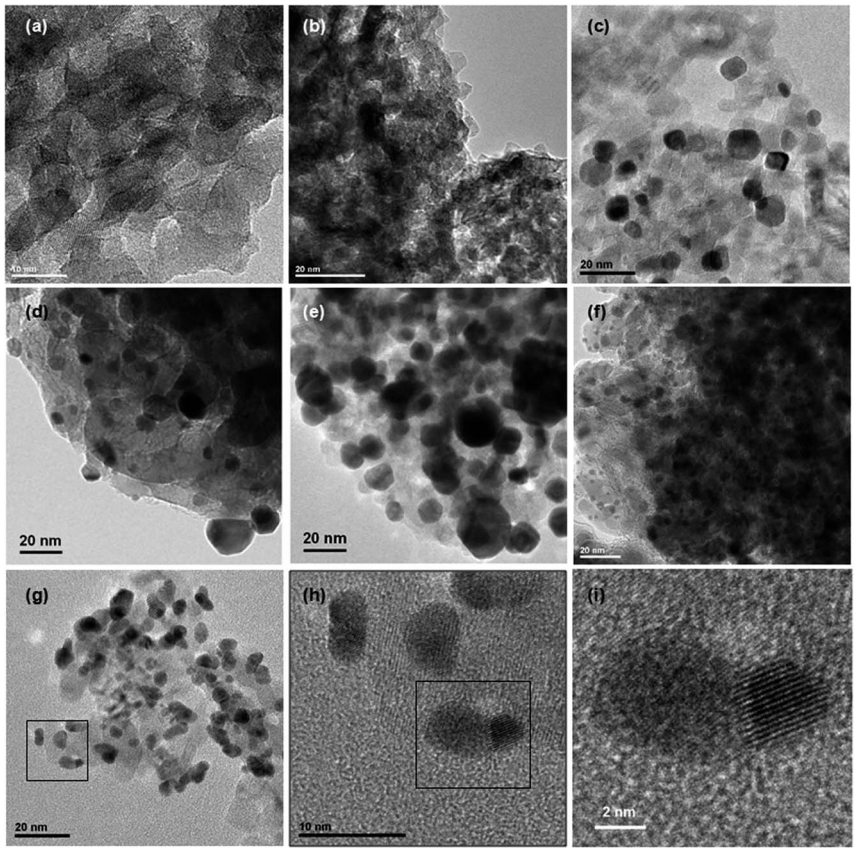

Fig. 3 TEM images of $Au5/TiO_2$ (a), $Pt5/TiO_2$ (b), $Au5Pt5/TiO_2$ (c), $Au7.5Pt7.5/TiO_2$ (d), $Au35/TiO_2$ (e), $Pt15/TiO_2$ (f), $Au17.5Pt17.5/TiO_2$ (g), zoomed-in images of the black squared regions in (g) and (h), showing a Janus-type Au–Pt structure, *i.e.* the presence of an Au/Pt interface (h and i, respectively).

TiO_2. Sub-nm cluster-type objects were observed in all 3 materials. A large enough population could be measured in $Pt5/TiO_2$ and a mean size of 0.4 ± 0.2 nm could be determined (Fig. 4a), clearly showing that the metallic phase in these materials exclusively consists of sub-nm clusters (except for $Au5/TiO_2$ which contains some large gold aggregates in addition to the sub-nm clusters). Hence supported clusters were successfully prepared in one pot by performing the thermal DMF reduction of gold and platinum salts, inspired from previous studies, in the presence of titania.[35–37]

X-ray photoelectron spectroscopy (XPS). $Au5/TiO_2$, $Pt5/TiO_2$, $Au2.5Pt2.5/TiO_2$, $Au5Pt5/TiO_2$, $Au7.5Pt7.5/TiO_2$ XPS spectra all show the $Ti2p_{1/2}$–$Ti2p_{3/2}$ doublet, with the $Ti2p_{3/2}$ peak located at 458.7 ± 0.1 eV, which is typical of anatase titania.[45] The $Au4f_{5/2}$–$Au4f_{7/2}$ doublet is also found in all Au-containing catalysts. Each peak can be fitted with a single component, containing a certain degree of asymmetry (Fig. S1†), which is typical of metallic Au NPs. The $Au4f_{7/2}$ peak is however positioned at 83.0 ± 0.3 eV, *i.e.* about 1 eV lower than in bulk gold ($Au4f_{7/2}$ at 84.0 eV). It is typical of metallic Au NPs in interaction with titania.[25] The slightly negative charge on Au NPs is due to equilibration of Fermi levels during

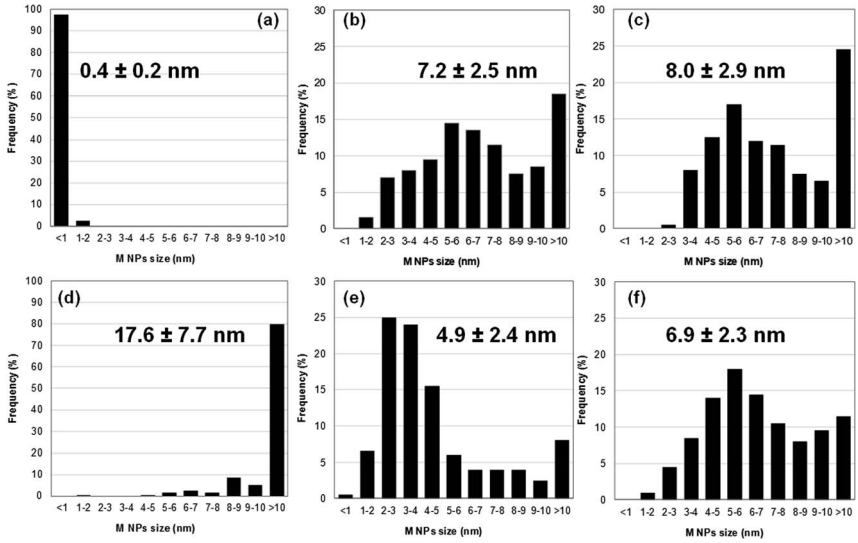

Fig. 4 TEM-derived metal NP-size distributions in Pt5/TiO_2 (a), Au5Pt5/TiO_2 (b), Au7.5Pt7.5/TiO_2 (c), Au35/TiO_2 (d), Pt15/TiO_2 (e), Au17.5Pt17.5/TiO_2 (f).

formation of the Au/TiO_2 Schottky junction which induces charge transfer from titania to Au NPs. Au5Pt5/TiO_2 and Au7.5Pt7.5/TiO_2 both exhibit an additional doublet corresponding to $Pt4f_{5/2}$–$Pt4f_{7/2}$. Each peak can be fitted with one single component, containing a certain degree of asymmetry (Fig. S1†), which is typical of metallic Pt. The $Pt4f_{7/2}$ peak is positioned at 70.0 ± 0.2 eV, which is 1 eV lower than the binding energy of the $4f_{7/2}$ core level electrons in bulk platinum metal ($Pt4f_{7/2}$ at 71.0 eV). Hence Pt NPs, like Au NPs, are in the metallic form only and electron-rich. Both a support effect, *i.e.* electron transfer from titania to Pt NPs,[46] and an alloy effect, *i.e.* electron transfer from gold to platinum,[47,48] can account for the low binding energy observed. For Pt5/TiO_2 and Au2.5Pt2.5/TiO_2, the Pt4f signal is much weaker and shifted to higher binding energies (Fig. S1†), which is attributed to the lower Pt content of these materials and a surface–core level shift effect due to the sub-nm cluster size of Pt.

Surface atomic ratios can be calculated from XPS data. The Ti/O ratio is found to be 0.53 ± 0.02 eV in all five catalysts (Table 2). It is close to the expected theoretical ratio of 0.5 in TiO_2. On the other hand, both the Au/Ti and Pt/Ti surface ratios vary. Interestingly, while the Pt/Ti surface ratio increases with increasing Pt/Ti bulk ratio (derived from the ICP data), the Au/Ti surface ratio varies independently from the bulk Au/Ti ratio and is much lower in the bimetallic catalysts, than in Au5/TiO_2. As a result, the Pt/Au surface ratios (1.3, 42 and 146, for Au2.5Pt2.5/TiO_2, Au5Pt5/TiO_2 and Au7.5Pt7.5/TiO_2, respectively) are found to be much higher than the Pt/Au bulk ratios (0.22, 0.98 and 1.22 for Au2.5Pt2.5/TiO_2, Au5Pt5/TiO_2 and Au7.5Pt7.5/TiO_2, respectively), *i.e.* 6 times higher in Au2.5Pt2.5/TiO_2, 43 times higher in Au5Pt5/TiO_2 and 119 times higher in Au7.5Pt7.5/TiO_2. This indicates massive Pt segregation on the surface and, more precisely, massive screening/coverage of the gold surface by Pt NPs larger than the inelastic mean free path of electrons (10–12 Å), which increases with increasing Pt content and Pt/Au bulk ratio.

Table 2 Atomic ratios

	Surface (XPS)				ICP (bulk)			Surface/bulk		
	Ti/O	Au/Ti	Pt/Ti	Pt/Au	Au/Ti	Pt/Ti	Pt/Au	Au/Ti	Pt/Ti	Pt/Au
$Au5/TiO_2$	0.52	0.10	0.00	—	0.0171	0	—	5.7	—	—
$Au2.5Pt2.5/TiO_2$	0.53	0.02	0.03	1.3	0.0080	0.0018	0.22	2.6	15.2	5.9
$Au5Pt5/TiO_2$	0.55	0.01	0.39	42	0.0186	0.0182	0.98	0.5	21.2	43
$Au7.5Pt7.5/TiO_2$	0.49	0.0048	0.70	146	0.0168	0.0206	1.22	0.3	34.3	119
$Pt5/TiO_2$	0.50	0	0.02	—	0	0.0016	—	—	15.0	—
$Au35/TiO_2$	0.51	1.53	0	0	0.2034	—	—	7.5	—	—
$Au34Pt1/TiO_2$	0.52	1.70	0.26	0.15	0.2121	0.0063	0.03	8.0	40.5	5.1
$Au30Pt5/TiO_2$	0.47	1.25	0.30	0.24	0.1808	0.0164	0.09	6.9	18.2	2.6
$Au17.5Pt17.5/TiO_2$	0.53	0.80	0.26	0.33	0.0954	0.0122	0.14	8.4	21.5	2.6
$Au3.5Pt3.5/TiO_2$	0.52	0.22	0.05	0.23	0.0117	0.0015	0.13	18.4	32.4	1.8
$Au5Pt30/TiO_2$	0.49	0.41	0.19	0.48	0.0216	0.0057	0.25	18.7	34.2	1.8
$Pt35/TiO_2$	0.48	0.00	1.54	—	—	0.0768	—	—	20.0	—

Optical properties. The optical properties of the materials were studied by diffuse reflectance UV-visible spectroscopy (Fig. 5a). UV-vis spectra all show the typical absorption band of 100% anatase TiO_2 between 200 and 380 nm. This band is used to normalize the visible response of the materials, which is due to the metallic phase/component, and more specifically to the presence of metallic nanoparticles. Absorption in the visible range can be attributed to the localized surface plasmon resonance (LSPR) of Au and Pt NPs, with a maximum at about 580 nm for Au NPs and a continuously decreasing absorbance over the visible range for Pt NPs, as observed in the spectra of $Au5/TiO_2$ and $Pt5/TiO_2$, respectively.[49–51] The red-shift in the LSPR position of Au NPs, as compared with those generally observed for Au colloids, is due to the titania matrix and suggests strong interactions between the metal NPs and the TiO_2 support.[25] The weak intensity of the LSPR in $Au5/TiO_2$ and $Pt5/TiO_2$ as compared with the Au and Pt reference samples ($0.9 \pm 0.1\%$ metal, 4 nm) is consistent with the presence of sub-nm clusters, as shown by SEM and TEM characterization of the materials (Fig. 2–4), considering the size-limit in LSPR

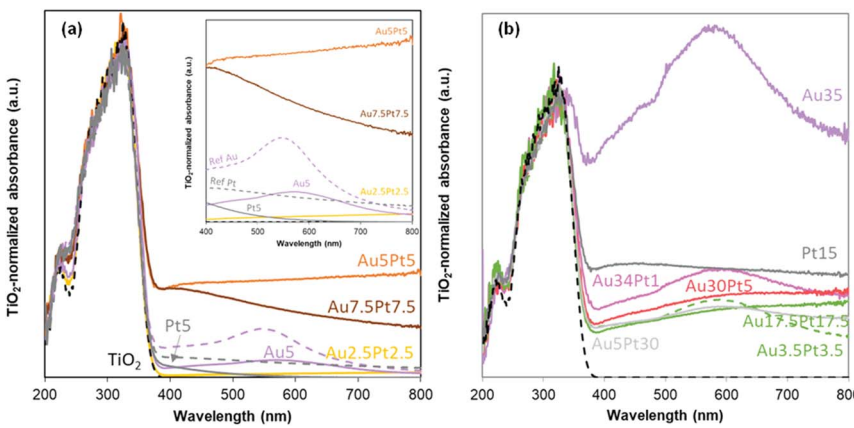

Fig. 5 UV-vis spectra of the Au–Pt/TiO_2 materials prepared by thermal DMF reduction (a) and by $NaBH_4$ reduction in DMF (b).

detection (2 nm). It confirms that the sub-nm cluster is the principle form of metal object present in the samples and that the number of aggregates in Au5/TiO_2 is quite small. It is noted that, for Pt5/TiO_2, the low Pt content (0.3%) may also contribute to the lower LSPR intensity as compared with the Pt reference. It is also noted that the relative intensities of the Pt and Au LSPRs in the reference samples (similar metal loadings, similar metal NP sizes) are in line with the higher absorption cross-section of gold as compared with platinum.[52]

In the bimetallic catalysts, absorption in the visible range is clearly and markedly dependent on the metallic composition. Absorption in the visible range is quite limited for Au2.5Pt2.5/TiO_2, and more specifically much smaller than in Au5/TiO_2 and Pt5/TiO_2. Given the far from negligible metal content of the material (2.3 wt%), the low visible absorption is consistent with Au and Pt NP size far below the LSPR size-limit detection, *i.e.* with the sub-nm cluster size and the absence of M NPs and aggregates evidenced by SEM and TEM. The more loaded catalysts (8.3–8.4 wt% metal) exhibit a much more significant absorption in the visible range. Intensity of the Pt NPs LSPR (420 nm) is much higher than in Pt5/TiO_2 due to higher Pt loading and larger NPs size distribution. The similarity in intensities of Pt NPs LSPR (420 nm) in both Au5Pt5/TiO_2 and Au7.5Pt7.5/TiO_2 is consistent with the similar Pt loadings measured (4.1 and 4.6 wt%, respectively). However absorption remains high at $\lambda >$ 420 nm in Au5Pt5/TiO_2, while it decreases in Au7.5Pt7.5/TiO_2. This can be attributed to a less pronounced contribution of Au NPs LSPR. It is attributed to efficient screening/quenching of the Au LSPR by Pt,[53] at the highest Pt/Au ratio (1.22) achieved in Au7.5Pt7.5/TiO_2, LSPR damping has been observed before in *e.g.* core–shell Au@Pt NPs.[52]

Catalytic properties for CO_2-to-CH_4 plasmon-induced reduction with water

Methane production rates obtained upon plasmonic excitation of the catalysts ($\lambda >$ 400 nm) over time are shown in Fig. 6a. Negligible rates are obtained using the monometallic catalysts (0–0.1 μmol h^{-1} g^{-1} on average over 5 h). In previous

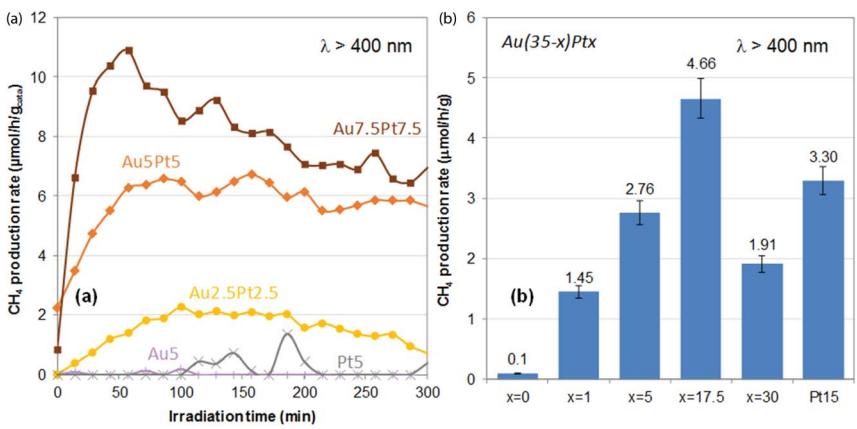

Fig. 6 Plasmon-induced methane production rates observed under visible light irradiation ($\lambda >$ 400 nm) over Au–Pt/TiO_2 catalysts prepared by thermal DMF reduction (a) and Au(35 − *x*)Pt*x*/TiO_2 catalysts prepared by $NaBH_4$ reduction in DMF (b). In (b), methane production rates are average production rates over 5 h of reaction (Table 1). Error bars represent the uncertainty generally observed on such values, *i.e.* 7% of the absolute value.

work, we showed that Au(1 wt%, 3 nm)/TiO_2 could produce about 0.3 μmol h^{-1} g^{-1} on average over 5 h.[28] The lower activity of the monometallic Au5/TiO_2 catalyst presented here is attributed to the much lower optical absorbance in the visible range. It also suggests that sub-nm Au (and Pt) clusters are not suitable plasmonic catalysts for the plasmon-induced reduction of CO_2 with water. On the other hand, the bimetallic catalysts all exhibit significant methane productions – 1.5 to 7.8 μmol h^{-1} g^{-1} on average over 5 h, which increase with increasing Pt loading and Pt/Au ratio (Table 1). A useful synergy between gold and platinum is thus at play in these materials. Au2.5Pt2.5/TiO_2 is indeed more active than both Au5/TiO_2 and Pt5/TiO_2, despite its lower optical absorbance (Fig. 5a). The most beneficial impact is found for Au7.5Pt7.5/TiO_2, which produces 7.8 μmol h^{-1} g^{-1} of methane on average over 5 h of illumination, with 100% selectivity, thus showing the best catalytic performance of both catalyst series (Table 1). Hence, Pt segregation on the gold surface, as evidenced by XPS, is clearly beneficial to the production of methane. This suggests that the bimetallic catalysts may operate like an antenna-reactor-type system,[54] in which the photon-derived energy and charges generated within the gold core are transferred to the platinum surface,[47,52] where the reaction takes place. Besides, over the materials containing sub-nm metal clusters (Au5/TiO_2, Pt5/TiO_2, Au2.5Pt2.5/TiO_2) hydrogen is produced from the competitive reduction of water, and the selectivity of Au2.5Pt2.5/TiO_2 for methane does not exceed 25%. On the other hand, no production of hydrogen is observed on the materials containing 7–8 nm metal NPs (Au5Pt5/TiO_2 and Au7.5Pt7.5/TiO_2), and methane is thus produced with 100% selectivity. This suggests that the size of the plasmonic NPs affects the selectivity of the reaction, and that promoting the reduction of CO_2 over the competitive reduction of water requires a certain metal NPs size. The higher loading of the plasmonic NPs in Au5Pt5/TiO_2 and Au7.5Pt7.5/TiO_2 (8.3–8.4 wt%) *vs.* Au5/TiO_2, Pt5/TiO_2, Au2.5Pt2.5/TiO_2 (≤4%) may also contribute to increase the selectivity.

Bimetallic catalysts prepared by $NaBH_4$ reduction in DMF

Deposition efficiency. Seven catalysts were prepared with this method: monometallic Au35/TiO_2 and Pt15/TiO_2 references, as well as four bimetallic Au(35 − *x*)Pt*x*/TiO_2 catalysts ($x = 1$, 5, 17.5, 30; *i.e.* targeted Pt/Au ratio of 0.03, 0.16, 1, 6, with the same targeted metal loading of 35 wt%), and Au3.5Pt3.5/TiO_2 (targeted Pt/Au ratio of 1, with targeted metal loading of 7 wt%).

In the gold-containing mono- and bi-metallic catalysts, the actual gold loadings determined by ICP-OES are close to the targeted gold loadings (Table 1 and Fig. 1b), and deposition yields are close to 100% for targeted loadings above 5 wt%, and about 80% for the targeted loading of 3.5 wt%. On the other hand, Pt is not efficiently deposited with this method. In the monometallic catalyst, no Pt is actually deposited without slightly modifying the synthesis protocol (see Experimental section). In the bimetallic catalysts, Pt loadings do not exceed 2.7 wt% (Table 1 and Fig. 1c), with deposition yields exponentially decreasing with increasing targeted Pt loadings and decreasing targeted Au loading (Fig. 1d). This shows that, like for thermal DMF reduction, gold enhances Pt deposition, which suggests that deposited gold NPs, or the Au/TiO_2 perimeter sites, may serve as nucleation sites for Pt. As a result, the targeted fixed metal loading of 35 wt% actually varies from 6.3 to 35 wt%, decreasing with decreasing gold content in the

Au(35 − x)Ptx/TiO_2 series, the range of Pt/Au ratios achieved is narrower than expected (0–0.25, instead of 0–6) and only gold-rich compositions are achieved (Pt/Au ratio < 0.25). Interestingly, due to the lower deposition yields of both Au and Pt in Au3.5Pt3.5/TiO_2, a similar Pt/Au ratio of 0.13–0.14 is obtained in both Au3.5Pt3.5/TiO_2 and Au17.5Pt17.5/TiO_2, associated with two significantly different metal loadings (3.2 and 19.9 wt%, respectively).

Metal NPs size and distribution over titania. Low magnification SEM images show the presence of large metal aggregates (100 nm to 1 μm) on Au35/TiO_2, Au17.5Pt17.5/TiO_2 and Au3.5Pt3.5/TiO_2 (Fig. 7). For the bimetallic catalysts, the size of the metal aggregates is clearly larger in the more loaded material. A large amount of smaller metallic NPs can be seen at higher magnification. Extensive coverage of the TiO_2 support with these smaller NPs can be observed for Au35/TiO_2 (Fig. 7a). Coverage appears to be quite high in Au3.5Pt3.5/TiO_2 (Fig. 7b) also. It appears lower for Au17.5Pt17.5/TiO_2 (in the selected region, Fig. 7c), which suggests that the larger aggregates may dominate in this material.

Size distributions of the smaller metallic NPs present in Au35/TiO_2, Pt15/TiO_2 and Au17.5Pt17.5/TiO_2 were obtained by measuring the lower dimension of 200

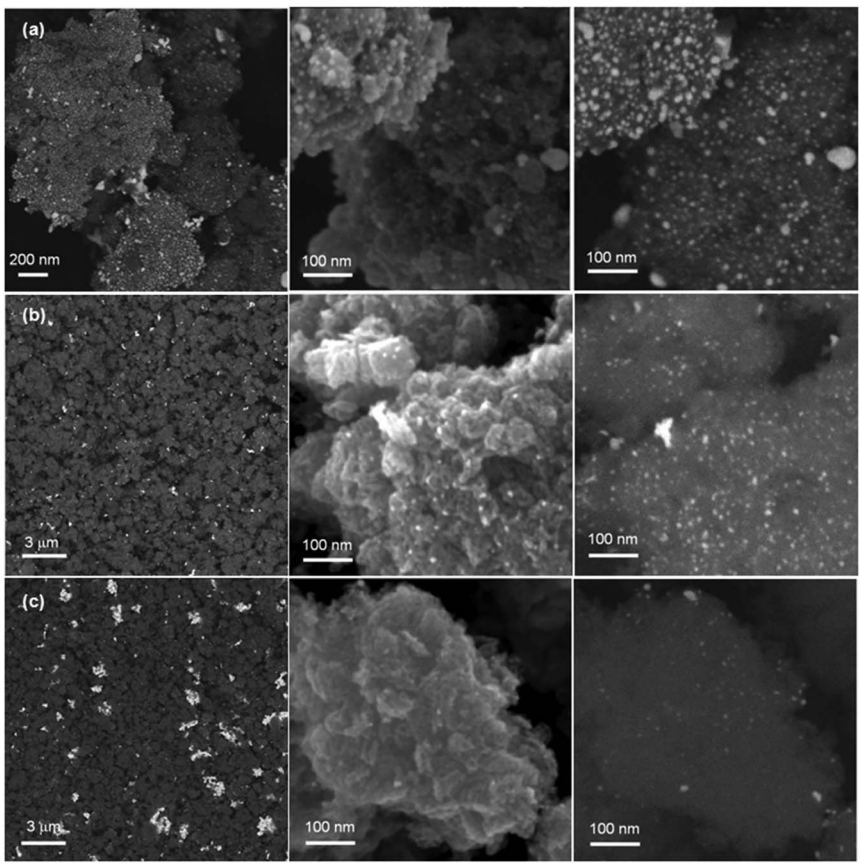

Fig. 7 SEM images of Au35/TiO_2 (a), Au3.5Pt3.5/TiO_2 (b), Au17.5Pt17.5/TiO_2 (c), at low magnification (left) and at high magnification, using In lens (middle) and BSE (left, right) detectors.

NPs on TEM images (Fig. 3e–g), in the case of oblong NPs. Like for the materials prepared by thermal DMF reduction, a significant amount of oblong metal NPs can be found in the bimetallic Au17.5Pt17/TiO_2 catalyst. Size distributions are presented in Fig. 4d–f. They are centered at 17.6 ± 7.7 nm for Au35/TiO_2, at 2–3 nm for Pt15/TiO_2 with a mean NPs size of 4.9 ± 2.4 nm, and at 5–6 nm for Au17.5Pt17.5/TiO_2 with a mean NPs size of 6.9 ± 2.3 nm. While mostly NPs > 10 nm are found in Au35/TiO_2, a significant amount of very small NPs (<1–3 nm, 32% of the counted population) can be found in the Pt15/TiO_2 catalyst. Au17.5Pt17.5/TiO_2 exhibits fewer NPs smaller than 3 nm (6% of the counted population) and more NPs larger than 10 nm (12%). However most of the NPs (82%) have sizes between 3 and 10 nm (Fig. 4f), evidencing the critical role of Pt in Au NPs size control in this method. Interestingly, Janus-type NPs were detected on Au17.5Pt17.5/TiO_2 (Fig. 3h, i and S2†). These Janus NPs consist of distinct Au and Pt nanocrystals sharing an interface, the Au nanocrystal being systematically larger than the Pt nanocrystal. The oblong shape of most of the metal NPs observed in the bimetallic Au17.5Pt17.5/TiO_2 catalyst suggests that a significant proportion could consist of Janus NPs. This is the first time that Au–Pt Janus NPs have been obtained by the one pot co-reduction of metal salts,[55] instead of multi-step seed-mediated growth.[56–58] Our one pot method makes use of the intrinsic properties of gold and platinum, namely the difference in reduction potential of the two metal species and the preferential reduction of gold species,[59] which favors the formation of phase segregated bi-metallic NPs with Pt on top of Au.[60]

X-ray photoelectron spectroscopy (XPS). XPS spectra of all the catalysts in this series show the $Ti2p_{1/2}$–$Ti2p_{3/2}$ doublet, with the $Ti2p_{3/2}$ peak appearing at 458.9 ± 0.1 eV, in agreement with pure anatase titania. All Au-containing catalysts also exhibit the typical $Au4f_{5/2}$–$Au4f_{7/2}$ doublet. Each peak can be fitted with a single component, containing a certain degree of asymmetry (Fig. S1†), which is typical of metallic Au NPs. The $Au4f_{7/2}$ peaks are positioned between 83.0 and 83.4 eV in all catalysts, which is typical of electron-rich metallic Au NPs in interaction with titania. All Pt-containing catalysts exhibit an additional multi-component signal in the $Pt4f_{5/2}$–$Pt4f_{7/2}$ region (Fig. S1†), indicating the presence of oxidized forms of Pt.[61] For $Pt4f_{7/2}$, the lower BE component positioned between 69.6 eV and 70.5 eV in all catalysts can be attributed to electron-rich metallic Pt. Electrons may be transferred from TiO_2 (upon alignment of the Fermi level during the Pt/TiO_2 junction formation) but also possibly from gold,[47,48] as suggested by the lower binding energy observed in the gold-containing catalysts as compared with monometallic Pt15/TiO_2.

Like for the materials prepared by thermal DMF reduction, platinum surface enrichment is observed by comparing Pt/Au surface ratios and Pt/Au bulk ratios (Table 2). The extent of the Pt enrichment is however more moderate, as Pt/Au surface ratios are indeed only 2 to 5 times higher than Pt/Au bulk ratios. This more moderate Pt surface enrichment is consistent with the Janus-type Au–Pt NPs observed by TEM (Fig. 3h and i) and the related partial coverage of Au surface by Pt NPs. It is attributed to a size effect, i.e. the larger size of Au NPs vs. Pt NPs (as evidenced e.g. for Au17.5Pt17.5/TiO2, see the TEM sub-section) considering the inelastic mean free path of electrons (10–12 Å).

Optical properties. The optical properties of the materials prepared by $NaBH_4$ reduction in DMF all contain the absorption band of the titania component in the UV range (200–380 nm), and a significant absorption in the visible region

(Fig. 5b). The monometallic Au35/TiO_2 and Pt15/TiO_2 catalysts exhibit the largest absorptions in the visible range, in line with their high metal loadings. The bimetallic catalysts all exhibit much lower absorptions in the visible range. In some cases (Au3.5Pt3.5/TiO_2, Au5Pt30/TiO_2), the decrease in intensity can be accounted for by the lower gold loadings (2.8–5 wt%) and even lower Pt loadings (0.4–1.3 wt%). However, the drastic difference in the intensities of the gold LSPR in Au34Pt1/TiO_2 and in Au35/TiO_2, which contain a similar amount of gold (33.4–34%), points to the occurrence of plasmon damping by Pt. Plasmon damping has been observed in other bimetallic structures.[49,52,62] It is interesting that it is induced/achieved here by only a very small amount of Pt (1 wt%, Pt/Au = 0.03). It suggests that, despite the low Pt amount, the interaction between gold and platinum is sufficient to severely impact the optical properties of gold and the LSPR signal in particular, in line with the modifications of the electronic properties of Pt probed by XPS. Damping of Au NPs LSPR further increases with increasing Pt/Au ratio, resulting in a further decrease in the visible absorption for Au30Pt5 and Au17.5Pt17.5/TiO_2 (Pt/Au ratios of 0.09 and 0.14, respectively). The LSPR of Au NPs still contributes to the overall visible absorption signal, as evidenced by a distinct absorption band with maximum at 580–600 nm in Au34Pt1/TiO_2 or by a steady increase in the absorbance from 400 to 800 nm in Au30Pt5/TiO_2 and Au17.5Pt17.5/TiO_2. This steady increase, which is not observed for Pt15 and which surpasses that observed for Au5Pt5/TiO_2 (see the section Bimetallic catalysts prepared by thermal DMF reduction), suggests that some parts of Au NPs are unmodified, in line with the more limited Au/Pt interface in these Janus-type NPs, as compared with a core-shell nanostructure, the larger size of Au *vs.* Pt NPs and the lower Pt/Au ratios.

Catalytic properties for CO_2-to-CH_4 plasmon-induced reduction

Methane production rates obtained on average over 5 h upon illumination of the catalysts with visible light ($\lambda > 400$ nm) are shown in Fig. 6b. Au35/TiO_2 produces a negligible amount of methane (0.1 μmol h^{-1} g^{-1}), despite its huge optical absorption in the visible range (Fig. 5b). This highlights the fact that an efficient light absorber is not necessarily an efficient plasmonic catalyst and that light absorption does not necessarily imply plasmon-induced activity. Plasmon-induced catalysis indeed relies on photogenerated charge carriers with very short lifetimes, the so-called "hot carriers" generated within the bulk of plasmonic NPs upon LSPR decay. To allow the catalytic reaction to proceed, the lifetime of these hot carriers need to be increased, by *e.g.* stabilization in the conduction band of an interfaced semi-conductor,[63,64] after which they will need to reach the surface. These phenomena are clearly facilitated in NPs with high surface-to-volume ratio NPs, which implies that a size effect can be expected on the plasmon-induced reaction. These phenomena also require a high-quality M/SC interface. Hence the much lower activity of Au35/TiO_2, as compared with that reported earlier for Au(1 wt%, 3 nm)/TiO_2 catalyst (0.3 μmol h^{-1} g^{-1}), can be attributed to the large size of the particles observed in Au35/TiO_2 (Fig. 7a), the quasi-absent population of small particles, which implies a low surface-to-volume ratio, as well as the poor interface with the nanocrystalline support (13 nm). The monometallic Pt15/TiO_2 catalyst exhibits a significant average methane production rate of 3.3 μmol h^{-1} g^{-1}, in line with its suitable NPs size (Fig. 3f and 4e) in

the range 2–10 nm. Most bimetallic catalysts exhibit methane production rates in-between those of Au35/TiO_2 (0.1 μmol h^{-1} g^{-1}) and Pt15/TiO_2 (3.3 μmol h^{-1} g^{-1}), only Au17.5Pt17.5/TiO_2 exhibits a higher average methane production rate of 4.7 μmol h^{-1} g^{-1}. The less evident synergistic effect between gold and platinum in these materials can be attributed to the prevalence of the poorly active gold phase, due to both the low Pt/Au ratios (0.03–0.25) and the lower coverage of the gold surface by platinum (see XPS sub-section and Table 2), *i.e.* to the more limited gold–platinum interface area. Utilization of the metal is clearly not optimal in these materials regarding the levels of CH_4 produced (Table 1); activity may be impeded by the presence of oxidized forms of Pt, in addition to the limited Au/Pt interface. Nevertheless, one has to keep in mind that the bimetallic catalysts all contain a much lower amount of platinum (1–2.7%, Table 1) than the monometallic Pt15/TiO_2 reference (15.8%). This shows that (1) the bimetallic catalysts are actually all more efficient than the monometallic reference on a Pt metal basis, highlighting the beneficial role of gold, and (2) a small amount of Pt, interfaced with Au, is sufficient to activate large inactive gold NPs. Besides, like for catalysts prepared by thermal DMF reduction, all materials containing a metal load above 6.3 wt% are 100% selective towards methane (no H_2 produced, Table 1). This supports the previous assumption that higher loadings of the plasmonic NPs, *i.e.* higher coverage of titania with plasmonic NPs, successfully promote CO_2 reduction over the competing water reduction reaction. None of the lower load catalysts (Au3.5Pt3.5/TiO_2 from $NaBH_4$ reduction and Au2.5Pt2.5/TiO_2 thermal DMF reduction) indeed reaches full selectivity towards methane (Table 1). Selectivity is nevertheless favored by the metal NPs present in Au3.5Pt3.5/TiO_2 rather than the sub-nm clusters present in Au2.5Pt2.5/TiO_2. However, methane production rates on a metal basis are clearly enhanced by the suitable Au/Pt nanoalloy core–shell structure achieved by thermal DMF reduction, rather than the Au/Pt Janus structure derived from $NaBH_4$ reduction.

Experimental

Synthetic procedures

$HAu(III)Cl_4 \cdot 3H_2O$ (99.99%), $NaAu(III)Cl_4 \cdot 2H_2O$ (99.99%), $H_2Pt(IV)Cl_6 \cdot xH_2O$ (99.999%), $K_2Pt(II)Cl_4$ (99.9%) were purchased from Alfa-Aesar and used without further purification. $NaBH_4$ (99%) was purchased from Sigma-Aldrich and used without further purification. DMF (99.9%) is purchased from Carlo Erba and used without further purification. TiO_2 Hombikat UV100 is purchased from Sachtleben Chemie and calcined in a muffle furnace for 4 h in air at 350 °C before use, to obtain a well-defined nanocrystalline pure anatase powder containing well-calibrated anatase crystallites (13 nm) in an aggregated form (SEM), displaying a surface area of 140 m^2 g^{-1} and no amorphous phase.

Thermal DMF reduction (DMF/140 °C). TiO_2 (1 g) is added to DMF (100 mL) and stirred for 5 min before being heated at 140 °C under vigorous stirring. After 5 min at 140 °C, an aqueous solution of $HAuCl_4$ (1 mL/0.25 M/50 mg Au) is added and the mixture is left to react for 4 h at 140 °C. The resulting slightly colored powder in suspension is isolated by filtration, washed (water/400 mL), dried (vacuum/100 °C/2 h) and calcined in air at 200 °C for 1 h, leading to Au5/TiO_2, where [5] stands for the targeted gold content in the dried sample in wt%.

$Pt5/TiO_2$ is synthesized in the same way, replacing $HAuCl_4$ by H_2PtCl_6 (1 mL/0.25 M/50 mg Pt).

A series of Au*x*Pt*y*/TiO_2 catalysts ($x = y = 2.5$, 5, 7.5) is prepared in the same way, replacing $HAuCl_4$ by the (quasi) simultaneous addition of both $HAuCl_4$ and H_2PtCl_6 aqueous solutions (0.25 M), adjusting the volume of the solutions to the target loading. *x* and *y* stand for the targeted gold and platinum content (wt%), respectively, in the dried samples.

$NaBH_4$ reduction in DMF (DMF/$NaBH_4$). TiO_2 (195 mg) is added to DMF (200 mL) and stirred for 5 min at room temperature (*ca.* 22 °C). A given amount of $NaAuCl_4$ crystalline powder is added and left to react for 5 min. $NaBH_4$ is then introduced (202 mg/$NaBH_4$/Au = 10) and left to react for 30 min. The colored powder in suspension is then isolated by filtration, washed (water/400 mL), dried (air/100 °C/24 h) and calcined in air at 200 °C for 1 h, leading to $Au35/TiO_2$, where [35] stands for the targeted gold content in the dried sample in wt%.

A series of Au(35 − *x*)Pt*x*/TiO_2 catalysts ($x = 0$, 1, 5, 17.5, 30) is prepared in the same way, replacing $NaAuCl_4$ by the (quasi) simultaneous addition of both $NaAuCl_4$ and K_2PtCl_4 crystalline powders, adjusting the weight of the powders to the target loading and using $NaBH_4$/(Au + Pt) = 10, where *x* stands for the targeted platinum content (wt%) in the dried samples.

A $Au3.5Pt3.5/TiO_2$ catalyst was prepared in the same way, by adjusting the weight of the powders to the target loading.

An attempt to prepare $Pt35/TiO_2$ by reacting K_2PtCl_4 alone under the conditions described for $NaAuCl_4$ did not lead to any Pt deposition on TiO_2, as evidenced by ICP-OES. After several attempts, we finally managed to prepare a monometallic Pt/TiO_2 reference as follows: TiO_2 (195 mg) is added to DMF (200 mL) and stirred for 5 min at room temperature (*ca.* 22 °C). K_2PtCl_4 (crystalline powder, 223.4 mg) is added and left to react for 5 min. $NaBH_4$ is then introduced (204 mg/$NaBH_4$/Pt = 10) and left to react for 30 min. The white powder in suspension is then isolated by filtration. The filtrate is left to settle overnight; a dark precipitate appears. The supernatant is sampled. The white powder is added to the supernatant under stirring and the mixture heated to 140 °C for 3 h. The powder in suspension that has turned grey is then isolated by filtration, washed (water/400 mL), dried (air/100 °C/24 h) and calcined in air at 200 °C for 1 h, leading to $Pt15/TiO_2$, where [15] stands for the actual Pt content in the dried sample in wt% as measured by ICP-OES.

Efficiency of the methods is discussed on the basis of the deposition yield of each metal, which is defined as the ratio between the metal content measured in the dried samples by ICP-OES (IPHC/UMR CNRS 7178) and the targeted metal content (given the amount of metal initially present in the solution).

Characterization

ICP-OES. Elemental analysis (ICP) of the composites was performed using inductively coupled plasma-optical emission spectroscopy (ICP-OES, Varian 720ES) at IPHC (CNRS UMR 7178, France).

UV-visible spectroscopy. UV-vis absorption spectra were recorded on a PerkinElmer 950 spectrophotometer fitted with a Labsphere RSA ASSY 100 nm integrating sphere. The spectra are acquired in reflection mode (diffuse reflectance). In order to determine the absorbance coefficient, the diffuse

reflectance spectra were converted to Kubelka–Munk units *via* the equation: $F(R) = (1 - R)^2/2R$.

X-ray photoelectron spectroscopy (XPS). XPS measurements were carried out in an ultrahigh vacuum (UHV) spectrometer equipped with a VSW Class WA hemispherical electron analyzer. A dual anode Al Kα X-ray source (1486.6 eV) was used as incident radiation. Survey and high resolution spectra were recorded in constant pass energy mode (90 and 20 eV, respectively, or 50 eV for the Au 4f and Pt 4f regions). All binding energies were referenced to the C 1s peak at 285.0 eV to compensate for the charge effect. % surface contents were calculated using the corresponding core level peaks, normalized to the photoemission cross-section and assuming a homogeneous distribution arrangement model. Surface atomic ratios are subsequently calculated on the basis of these values. Deconvolution of the C 1s, O 1s Ti 2p, Au 4f and Pt 4f core level peaks was achieved with CASA XPS Software using a Shirley background and peak shapes, linewidths (FWHM), intensity ratios and separation of spin–orbit components previously established in the literature.

Scanning electron microscopy. Scanning electron microscopy (SEM) was carried out on a Zeiss Gemini SEM 500 system at 6 kV using a working distance (WD) of 3.5 mm and an aperture (AP) of 30 μm. Two detectors were used alternatively: an in lense secondary electron detector (In Lens) for best imaging resolution, and a back-scattered electrons (BSE) detector providing chemical contrast, with the lightest elements (Ti) appearing darker than the heaviest elements (Au, Pt). The powder samples were pressed on a sample holder decorated with carbon tape before analysis.

Transmission electron microscopy. Transmission electron microscopy (TEM) was carried out on a JEOL 2100F microscope working at 200 kV accelerating voltage and equipped with a probe corrector for spherical aberrations, giving a point-to-point resolution of 0.18 nm. The sample was dispersed by ultrasound in an ethanol solution for 2 min. A drop of the solution is subsequently deposited on copper covered with a holey carbon membrane and left to dry at ambient temperature (22 °C) before observation. Size distributions are obtained by measuring the size of 200 particles using the ImageJ software.[65]

Catalytic evaluation. The photocatalytic set-up designed for gas phase photoreduction of CO_2 with water was described previously.[28] It is made of 1/16″ stainless steel lines. The low CO_2 flow (air product, 99.5%) is controlled by a dedicated mass-flow controller (Bronkhorst) allowing us to control flow rates as low as 0.3 mL min^{-1}. It is loaded with gas phase water by passing through a temperature-controlled 3 mL water saturator which is maintained at 28 °C in order to get a steady absolute humidity of about 4%. The continuously flowing reaction mixture (CO_2 + H_2O) then passes through the metallic circular photoreactor cell (6 mL) equipped with a welded gas inlet and welded gas outlet on the sides, and a 3 mm-thick Quartz window from Verlabo2000 (France) on top. The photoreactor is irradiated with a 150 W ceramic-metal-halide Hg lamp top-irradiation system with light concentrator placed 6 cm above the Quartz window. The emission spectrum is given in Fig. 8. Total irradiance is 5100 W m^{-2}, corresponding to a photon flux of 0.028 mol s^{-1} m^{-2}. The total irradiated surface is 18.8 cm^2. For evaluation under so-called "visible light", *i.e.* evaluation of the plasmon-induced catalytic performances, a Schott GG 400 optical filter from Edmund Optics is placed between the photoreactor and the light source to cut all wavelengths below 400 nm. The irradiance is 4800 W m^{-2} for the whole spectrum

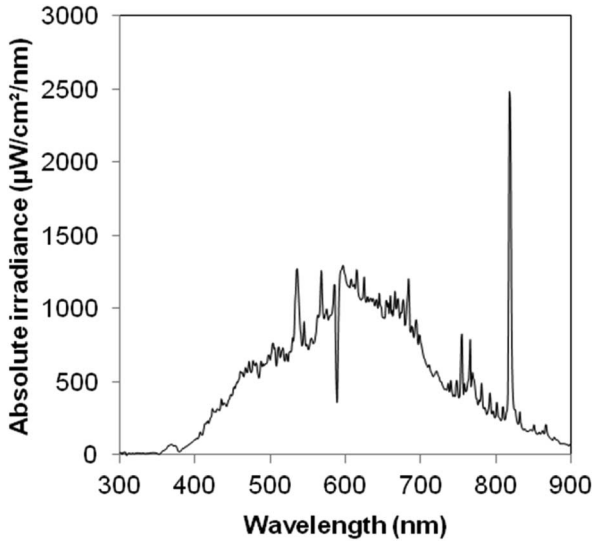

Fig. 8 Emission spectrum of the 150 W ceramic-metal-halide Hg lamp.

with a filter (400–900 nm), corresponding to a photon flux of 0.025 mol s^{-1} m^{-2}. On-line gas analysis is performed by gas chromatography using an Agilent 3000A SRA Instrument micro-GC equipped with 4 channels (Channel A: MolSieve-5 Å, Ar, $l = 10$ m, $T = 90$ °C for detection of H_2, CH_4, O_2, N_2, CO; Channel B: PLOTU, He, $l = 8$ m, $T = 75$ °C, for detection of CO_2; Channel C: STABILWAX, He, $l = 10$ m, $T = 80$ °C, for possible detection of C_2H_4; Channel D: OV1, He, $l = 34$ m, $T = 80$ °C, for detection of H_2O). The gas mixture is analyzed every 14 min for at least 5 h. Lower detection limits for H_2 and CH_4 are 1.7 vol ppm and 0.9 vol ppm, respectively, under these conditions. Methane production rates are calculated using r_{CH_4} (μmol h^{-1} g^{-1}) = [CH_4] × (flow rate) × 60/(V_m × $m_{photocat}$), where [CH_4] is the concentration of CH_4 in ppm, $m_{photocat}$ is the mass of photocatalyst, the flow rate is 0.0003 L min^{-1} and $V_m = 24.79$ L mol^{-1} (STP conditions). Selectivity is $(8 \times r_{CH_4})/(8 \times r_{CH_4} + 2 \times r_{H_2}) \times 100$, as CH_4 and sometimes H_2 are the only two products detected under these conditions.

Conclusions

Successful deposition of bimetallic Au–Pt sub-nm clusters on titania has been achieved in one pot by the thermal DMF co-reduction of gold and platinum salts in the presence of titania. The formation of sub-nm clusters is concentration-dependent. 7–8 nm NPs are formed at higher concentrations. Pt deposition is clearly occurring on gold, leading to fully metallic Au@Pt core–shell-type NPs. By comparison, titania-supported bimetallic Au–Pt NPs synthesized by $NaBH_4$ reduction in DMF exhibit a less extensive Au–Pt interface, resulting from Janus-type nanostructures, and oxidized forms of Pt. For both types of bimetallic structures, a clear synergistic effect between gold and platinum is observed in the continuous flow gas phase CO_2 reduction with water under visible light. Addition of platinum makes Au NPs more active and unselective gold clusters more

selective towards the reduction of CO_2 *vs.* the competing reduction of water. These properties rely on the presence of an interface between Au and Pt. Activity is further boosted in the core–shell like nanostructures obtained by DMF thermal reduction, due to maximized Pt surface segregation and Au-Pt interface area, while selectivity clearly benefits from high loading of the plasmonic metal NPs, *i.e.* large coverage of the titania support with plasmonic NPs.

Author contributions

L. H.: investigation, formal analysis, visualization; C. S.: investigation; J. T.: funding acquisition, supervision; T. H.: funding acquisition, supervision; V. K.: resources, supervision, writing – review and editing; V. C. conceptualization, funding acquisition, project administration, resources, supervision, validation, writing – original draft.

Conflicts of interest

There are no conflicts to declare.

Acknowledgements

This project has received financial support from the CNRS through the MITI interdisciplinary programs (SelCO2PlasmonRed project). This work of the Interdisciplinary Thematic Institute HiFunMat, as part of the ITI 2021–2028 program of the University of Strasbourg, CNRS and INSERM UMR 1121, was supported by IdEx Unistra (ANR-10-IDEX-0002) and SFRI (STRAT'US project, ANR-20-SFRI-0012) under the framework of the French Investments for the Future Program. L. H., J. T. and T. H. are grateful to the Centre islamique d'orientation et de l'enseignement supérieur (CIOES) for PhD fellowships. The French GDR OrNano and GDR Plasmonique active networks are gratefully acknowledged to have allowed fruitful and inspiring discussions about these results. Dr T. Dintzer (UMR CNRS 7515) and D. Ihiawakrim (UMR CNRS 7504) are thanked for acquiring SEM and TEM images respectively. Dr V. Papaefthimiou (UMR CNRS 7515) is thanked for acquiring XPS data.

Notes and references

1 R. Ferrando, J. Jellinek and R. L. Johnston, *Chem. Rev.*, 2008, **108**, 845.
2 H. B. Liu, U. Pal and J. A. Ascencio, *J. Phys. Chem. C*, 2008, **112**, 19173.
3 J. Luo, M. M. Maye, V. Petkov, N. N. Kariuki, L. Wang, P. Njoki, D. Mott, Y. Lin and C.-J. Zhong, *Chem. Mater.*, 2005, **17**, 3086.
4 H. Zhang and N. Toshima, *J. Colloid Interface Sci.*, 2013, **394**, 166.
5 R. J. Wong, J. Scott, P. Kappen, G. K.-C. Low, J. N. Hart and R. Amal, *Catal. Sci. Technol.*, 2017, **7**, 4792.
6 D. Zhao, Y.-H. Wang and B.-Q. Xu, *J. Phys. Chem. C*, 2009, **113**, 20903.
7 C. Jin, J. Zhu, R. Dong and Q. Huo, *Electrochim. Acta*, 2016, **190**, 829.
8 D. Zhao and B.-Q. Xu, *Phys. Chem. Chem. Phys.*, 2006, **8**, 5106.
9 D. Zhao and B.-Q. Xu, *Angew. Chem., Int. Ed.*, 2006, **45**, 4955.

10 G. Selvarani, S. V. Selvaganesh, S. Krishnamurthy, G. V. M. Kiruthika, P. Sridhar, S. Pitchumani and A. K. Shukla, *J. Phys. Chem. C*, 2009, **113**, 7461.
11 V. Petkov, B. N. Wanjala, R. Loukrakpam, J. Luo, L. Yang, C.-J. Zhong and S. Shastri, *Nano Lett.*, 2012, **12**, 4289.
12 J. Zhang, K. Sasaki, E. Sutter and R. R. Adzic, *Science*, 2007, **315**, 220.
13 B. N. Wanjala, J. Luo, R. Loukrakpam, B. Fang, D. Mott, P. N. Njoki, M. Engelhard, H. R. Naslund, J. K. Wu, L. Wang, O. Malis and C.-J. Zhong, *Chem. Mater.*, 2010, **22**, 4282.
14 N. S. K. Gowthaman and S. Abraham John, *RSC Adv.*, 2015, **5**, 42369.
15 Y. Yamauchi, A. Tonegawa, M. Komatsu, H. Wang, L. Wang, Y. Nemoto, N. Suzuki and K. Kuroda, *J. Am. Chem. Soc.*, 2012, **134**, 5100.
16 N. S. K. Gowthaman and S. Abraham John, *J. Chem. Sci.*, 2016, **128**, 331.
17 Z. Liu, H. Forsyth, N. Khaper and A. Chen, *Analyst*, 2016, **141**, 4074.
18 A. Gołąbiewska, W. Lisowski, M. Jarek, G. Nowaczyk, A. Zielińska-Jurek and A. Zaleska, *Appl. Surf. Sci.*, 2014, **317**, 1131.
19 A. Zaleska-Medynska, M. Marchelek, M. Diak and E. Grabowska, *Adv. Colloid Interface Sci.*, 2016, **229**, 80.
20 S. Shuang and Z. Zhang, *Molecules*, 2018, **23**, 525.
21 Z. K. Zheng, T. Tachikawa and T. Majima, *J. Am. Chem. Soc.*, 2014, **136**, 6870.
22 H. Song, X. Meng, T. D. Dao, W. Zhou, H. Liu, L. Shi, H. Zhang, T. Nagao, T. Kako and J. Ye, *ACS Appl. Mater. Interfaces*, 2018, **10**, 408.
23 X. Q. Yang, Y. Lu, Y. Liu, J. Wang, L. Shao and J. F. Wang, *Small Struct.*, 2021, **2**(12), 2100101.
24 B. N. Wanjala, J. Luo, B. Fang, D. Mott and C.-J. Zhong, *J. Mater. Chem.*, 2011, **21**, 4012.
25 P. Lignier, M. Comotti, F. Schüth, J.-L. Rousset and V. Caps, *Catal. Today*, 2009, **141**, 355.
26 K. Guillois, L. Burel, A. Tuel and V. Caps, *Appl. Catal., A*, 2012, **415**, 1.
27 F. Vigneron, A. Piquet, W. Baaziz, P. Ronot, A. Boos, I. Janowska, C. Pham-Huu, C. Petit and V. Caps, *Catal. Today*, 2014, **235**, 90.
28 S. Bardey, A. Bonduelle-Skrzypczak, A. Fécant, Z. Cui, C. Colbeau-Justin, V. Caps and V. Keller, *Faraday Discuss.*, 2019, **214**, 417.
29 L. Michel, S. Sall, T. Dintzer, A. Demange, C. Robert and V. Caps, *Faraday Discuss.*, 2021, **227**, 259.
30 P. Jiménez-Calvo, L. Michel, V. Keller and V. Caps, *ACS Appl. Mater. Interfaces*, 2021, **13**, 61015.
31 M. Khalid, N. Wasio, T. Chase and K. Bandyopadhya, *Nanoscale Res. Lett.*, 2010, **5**.
32 L. Qian, Y. Sha and X. Yang, *Thin Solid Films*, 2006, **515**, 1349.
33 S. Guo, J. Zhai, Y. Fang, S. Dong and E. Wang, *Chem.–Asian J.*, 2008, **3**, 1156.
34 L. Cao, L. Tong, P. Diao, T. Zhu and Z. Liu, *Chem. Mater.*, 2004, **16**, 3239.
35 X. Liu, C. Li, J. Xu, J. Lv, M. Zhu, Y. Guo, S. Cui, H. Liu, S. Wang and Y. Li, *J. Phys. Chem. C*, 2008, **112**, 10778.
36 H. Kawasaki, H. Yamamoto, H. Fujimori, R. Arakawa, Y. Iwasaki and M. Inada, *Langmuir*, 2010, **26**, 5926.
37 H. Kawasaki, H. Yamamoto, H. Fujimori, R. Arakawa, M. Inada and Y. Iwasaki, *Chem. Commun.*, 2010, **46**, 3759.
38 M. Hyotanishi, Y. Isomura, H. Yamamoto, H. Kawasaki and Y. Obora, *Chem. Commun.*, 2011, **47**, 5750.

39 Y. Isomura, T. Narushima, H. Kawasaki, T. Yonezawa and Y. Obora, *Chem. Commun.*, 2012, **48**, 3784.
40 K. Oikawa, S. Itoh, H. Yano, H. Kawasaki and Y. Obora, *Chem. Commun.*, 2017, **53**, 1080.
41 M. M. Heravi, M. Ghavidel and L. Mohammadkhani, *RSC Adv.*, 2018, **8**, 27832.
42 X. Chang, T. Wang and J. Gong, *Energy Environ. Sci.*, 2016, **9**, 2177.
43 W.-J. Yin, B. Wen, Q. Ge, X.-B. Li, G. Teobaldi and L.-M. Liu, *Dalton Trans.*, 2020, **49**, 12918.
44 R. Verma, R. Belgamwar and V. Polshettiwar, *ACS Mater. Lett.*, 2021, **3**, 574.
45 N. Satoh, T. Nakashima and K. Yamamoto, *Sci. Rep.*, 2013, **3**, 1959.
46 B. A. Sexton, A. E. Hughes and K. Foger, *J. Catal.*, 1982, **77**, 85.
47 C. Engelbrekt, K. T. Crampton, D. A. Fishman, M. Law and V. A. Apkarian, *ACS Nano*, 2020, **14**, 5061.
48 C.-E. Kim, D.-H. Lim, J. H. Jang, H. J. Kim, S. P. Yoon, J. Han, S. W. Nam, S.-A. Hong, A. Soon and H. C. Ham, *J. Chem. Phys.*, 2015, **142**, 034707.
49 D. Manchon, J. Lermé, T. Zhang, A. Mosset, C. Jamois, C. Bonnet, J.-M. Rye, A. Belarouci, M. Broyer, M. Pellarin and E. Cottancin, *Nanoscale*, 2015, **7**, 1181.
50 C. Langhammer, Z. Yuan, I. Zorić and B. Kasemo, *Nano Lett.*, 2006, **6**, 833.
51 M. Cueto, M. Piedrahita, C. Caro and B. Martínez-Haya, *J. Phys. Chem. C*, 2014, **118**, 11432.
52 A. Joplin, S. A. Hosseini Jebeli, E. Sung, N. Diemler, P. J. Straney, M. Yorulmaz, W.-S. Chang, J. E. Millstone and S. Link, *ACS Nano*, 2017, **11**, 12346.
53 N. Danielis, L. Vega, G. Fronzoni, M. Stener, A. Bruix and K. M. Neyman, *J. Phys. Chem. C*, 2021, **125**, 17372.
54 D. F. Swearer, H. Zhao, L. Zhou, C. Zhang, H. Robatjazi, J. M. P. Martirez, C. M. Krauter, S. Yazdi, M. J. McClain, E. Ringe, E. A. Carter, P. Nordlander and N. J. Halas, *Proc. Natl. Acad. Sci. U. S. A.*, 2016, **113**, 8916.
55 J. Qiu, Q. N. Nguyen, Z. Lyu, Q. Wang and Y. Xia, *Adv. Mater.*, 2022, **34**, 210259.
56 C. C. Crane, J. Tao, F. Wang, Y. Zhu and J. Chen, *J. Phys. Chem. C*, 2014, **118**, 28134.
57 I. Santiago, L. Jiang, J. Foord and A. J. Turberfield, *Chem. Commun.*, 2018, **54**, 1901.
58 J. Qiu, M. Xie, Z. Lyu, K. D. Gilroy, H. Liu and Y. Xia, *Nano Lett.*, 2019, **19**, 6703.
59 H. Ataee-Esfahani, L. Wang, Y. Nemoto and Y. Yamauchi, *Chem. Mater.*, 2010, **22**, 6310.
60 B. Klebowski, J. Depciuch, M. Stec, D. Krzempek, W. Komenda, J. Baran and M. Parlinska-Wojtan, *Int. J. Mol. Sci.*, 2020, **21**, 9610.
61 E. I. Vovk, A. V. Kalinkin, M. Yu. Smirnov, I. O. Klembovskii and V. I. Bukhtiyarov, *J. Phys. Chem. C*, 2017, **121**, 17297.
62 J. E. S. van der Hoeven, T.-S. Deng, W. Albrecht, L. A. Olthof, M. A. van Huis, P. E. de Jongh and A. van Blaaderen, *ACS Omega*, 2021, **6**, 7034.
63 P. Christopher and M. Moskovits, *Annu. Rev. Phys. Chem.*, 2017, **68**, 379.
64 L. Du, A. Furube, K. Yamamoto, K. Hara, R. Katoh and M. Tachiya, *J. Phys. Chem. C*, 2009, **113**, 6454–6462.
65 C. A. Schneider, W. S. Rasband and K. W. Eliceiri, *Nat. Methods*, 2012, **9**, 671.